Cellulose (2022) 29:9637–9655
https://doi.org/10.1007/s10570-022-04852-8

ORIGINAL RESEARCH

Cellulose and chitosan biopolymer composites reinforced with graphene and their adsorption properties for basic blue 41

Betul Cicek Ozkan

Received: 7 June 2022 / Accepted: 13 September 2022 / Published online: 23 September 2022

Abstract Chitosan/cellulose (CH/CE/GA) and chitosan/cellulose/graphene (CH/CE/G/GA) composites crosslinked via glutaraldehyde were used for the efficient adsorption of basic blue 41 (BB). FT-IR and ^{13}C solid-state NMR spectroscopy confirmed the crosslinking reaction of chitosan via glutaraldehyde, whereas XRD and TGA analysis proved the interactions between chitosan, cellulose, and graphene in the composites. FE-SEM and AFM studies provided evidence for the changes in the morphological and topological properties of the composites due to crosslinking reactions. Introducing graphene into the composites improved the specific surface areas, which led to enhanced thermal stability, swelling ratio, and dye adsorption capacity. The BB adsorption ability of the prepared crosslinked composites was investigated based on contact time, initial BB concentration, pH, and temperature. The Langmuir adsorption isotherm model was better fitted to the adsorption data of the composites relative to the Freundlich isotherm model. The pseudo-second-order kinetic model better correlates the adsorption of BB onto the prepared composites. The maximum adsorption capacity of CH/CE/GA was calculated as 107.87 mg/g using the Langmuir isotherm model, achieving a relatively higher maximal adsorption value of 129.3 mg/g with the CH/CE/G/GA composite after introducing graphene. Furthermore, the prepared composites demonstrated efficient BB adsorption properties and could be offered as environmentally friendly, stable materials for dye removal in wastewater treatments.

Keywords Cellulose · Chitosan · Graphene · Crosslinking · Basic blue 41 · Adsorption

B. Cicek Ozkan (✉)
Department of Metallurgical and Materials Engineering, Technology Faculty, Fırat University, 23119 Elazig, Turkey
e-mail: betulcckzkn@gmail.com; bcozkan@firat.edu.tr

Introduction

The growing textile industry in Turkey has been one of the sources of water pollution due to the rate of textile wastewater entering the natural environment. This is a major environmental concern because it has led to mucilage in the Marmara Sea, threatening living organisms. Over 100,000 different dyes, with azo dyes constituting over 50% of them are commercially available in the textile industry. Thus, textile effluents that contain azo dyes are undesirable due to their color, complex aromatic structures, and can be reduced into carcinogenic aromatic amines (Bianco Prevot et al. 2008; Pinheiro et al. 2004). Water pollution affects organisms that live in water; hence considerable attention should be paid to the control, removal, and treatment of dyes in wastewater before discharge. Several methods have been reported for the removal of dye from water, including adsorption, precipitation, filtration, and ion exchange (Firdaus et al.

2021). Among these methods, adsorption is the most promising technique for water treatments because of its low cost, higher dye uptake capacity, and reusability (Ali et al. 2020).

The need for disposable materials, and rapid social and economic development have increased environmental pollution and this threatens the survival of living things. The demand to replace synthetic polymer materials with products derived from natural resources such as cellulose (CE), chitosan (CH), gelatin, and lignin is increasing with research and reports aimed at overcoming the problem of pollution and climate change (Islam et al. 2020; Tran and Mututuvari, 2015). Compared to oil-based polymers, biopolymers have various advantages, such as biodegradability, biocompatibility, reproducibility, environmentally friendliness, and the emission of fewer greenhouse gasses (Mokhothu and John, 2015; Valizadeh et al. 2019). Cellulose and chitosan are the first and second most abundant and renewable biopolymer materials. They are suitable for producing composite materials for several applications, including drug delivery systems (Harkins et al. 2014), packaging (Demitri et al. 2016), coating (Jena et al. 2020), membranes (Aguirre-chagala et al. 2017), implants (Zhong et al. 2015), tissue engineering (Latifi et al. 2018), wound dressing (Alavi and Nokhodchi, 2020), water purification (Zhao et al. 2019), dye removal systems (Xu et al. 2021), and intelligent textiles (Shahid-ul-Islam et al. 2020et al. 2020).

Moreover, an essential property of chitosan is having natural functionality related to multiple reactive sites consisting of hydroxyl and amine groups, which makes the derivatization of material structures possible (Çiçek Ozkan, 2021). Additionally, chitosan possesses several excellent properties, including biodegradability, hydrophilicity, biocompatibility, chemical/physical functionality, high adsorption capacity, and antibacterial activity for various applications (Hassanein et al. 2017). For example, the functionalized chitosan-epichlorohydrin/kaolin clay composite was used to remove and reduce the chemical oxygen demand of reactive blue 19 dye from the aqueous solution (Jawad et al. 2020). On the other hand, the use of chitosan in an extensive field of application was restricted by its poor mechanical properties (Abdul Khalil et al. 2016).

Cellulose is the most abundant natural polymer material synthesized by major natural resources such as bacteria, fungi, marine animals, and plants. With the growing interest in nature-friendly, biocompatible, renewable, sustainable, and biodegradable materials, the importance of cellulose as an excellent alternative to petrol-based products has increased. The hydroxyl groups in cellulose can form hydrogen bonds within cellulose chains, improving thermal and mechanical properties (Askeland et al. 2011; Sharma et al. 2019). Cellulose nanofibers can also be produced using natural biomaterial wastes, including chestnut seed shells, pomelo peels, and horse chestnut seed shells, with promising properties for environmental remediation (Çiçek Özkan and Güner, 2022; Tang et al. 2020).

Although cellulose and chitosan have similar structures, they differ from each other with respect to an amine group that only exists in the chitosan chemical scaffold and presents it with unique properties (Stefanescu et al. 2012). Biopolymer composites have gained attention in developing sustainable and low-cost advanced materials for various applications and research. Among these biocomposites, chitosan and cellulose-based ones have attracted great interest for their excellent properties that are incorporated into the product. Cross-linking of chitosan improves its mechanical properties, chemical stability, and hydrophobicity of composites, decreasing the solubility in acidic media, leachability, and swelling capacity in the aqueous medium. The limiting effect of the cross-linking reaction decreases or increases depending on the concentration of the crosslinker, physicochemical properties, and the procedure used for the reaction (Jawad et al. 2019). Glutaraldehyde (GA) is widely used as a crosslinker due to its relatively low price and quick reaction (Udoetok et al. 2016). The functional reactivity of chitosan via NH_2 groups allows facile cross-linking with a crosslinker such as GA (Leung, 2001).

Graphene (G) can be dispersed into a biopolymer matrix to obtain novel materials (Bodur et al. 2020; Yigit et al. 2020). The functionality and enhanced features of composites based on chitosan, cellulose, and graphene have been investigated in numerous studies. For example, chitosan, graphene oxide, and carboxymethyl cellulose globules were produced to improve the adsorption ability and structural stability of materials (Huang et al. 2019). Mittal et al. fabricated a G/CH composite exhibiting increased thermal and mechanical properties (2017). Liu et al. investigated the adsorption properties of graphene for the

removal of methylene and concluded that graphene was a promising adsorbent (2012).

The superior properties of graphene, good mechanical, adsorption, and chemical structure properties of cellulose and antibacterial, biocompatible properties, and functional amine groups of CH can be cross-linked or blended to produce novel trio bio-nano composites with enhanced properties. Related researches show an increase in the mechanical, microstructure, surface, swelling, and sorption ability of such composite materials, creating new polymer architectures. For example, Azarniya et al. showed that increasing the concentration of graphene oxide affected and tailored the CH bacterial cellulose composites (2016). Chen et al. fabricated plasticized chitosan/carboxymethyl cellulose/reduced graphene oxide/graphene oxide composites with glycerol, which improved surface hydrophilicity, and decreased mechanical properties by adding nano-powders (2020). Cellulose-graphene nanoplatelets beads were employed for congo red adsorption by González-López et al. It was determined that the graphene nanoplatelets beads enhanced the adsorption and kinetic rates (González-López et al. 2021). In another report, chitosan gelatin composite was filled with graphene for adsorption of orange II dye and the graphene-contained composite was described as a promising adsorbent for potential applications in wastewater treatment (Wu et al. 2019).

The physicochemical, mechanical, and adsorptive properties of composites can be altered via physical and chemical interactions for various applications. For materials that have physically interacted, the newly produced composite material possesses unique features of its precursor and improves its adsorption behavior and recyclability. Along with physical interactions, a fundamental change occurs in the composite structure because of the chemical cross-linking reaction with GA, resulting in decreased solubility in acidic media, increasing mechanical properties, and chemical stability. However, physically and hybrid physically-chemically interacted chitosan, cellulose, and graphene composites have not been reported regarding structural, thermal, surface, textural, morphology, topology, water uptake, and dye adsorption properties. In this context, the novel chitosan/cellulose (isolated from the shell of horse chestnut seed) and chitosan composites reinforced with graphene were synthesized by a simple solution mixing and casting method. This work has contributed to advanced material research in many ways: (i) the extraction of cellulose from horse chestnut in order to put natural waste to good use, (ii) the design and manufacture of valuable biopolymer composites using inexpensive and superior biopolymers and graphene, (iii) the effect of nanographene particles on adsorption properties of biopolymer composites concerning pH sensitivity, temperature, initial basic blue 41 (BB) concentration, and contact time.

Experimental

Materials

Graphene nanoplatelets (Purity: 99.9%, Size: 3 nm, S.A: 800 m^2/g, Dia: 1.5 µm) were purchased from Nanografi. Low molecular weight CH (1526.5 g/mol molecular weight and 75–80% deacetylation degree) and basic blue 41 (BB) were purchased from Sigma-Aldrich. Sulfuric acid (H_2SO_4 95.0–98.0 wt.%, Vetec, P.A.), sodium chlorite ($NaClO_2$, technical grade, 80%, Sigma–Aldrich), absolute acetic acid (Sigma–Aldrich), sodium hydroxide (NaOH, Sigma–Aldrich), and sodium dihydrogen phosphate dehydrate (NaH_2PO_4*$2H_2O$, Merck Millipore) were used as received.

Extraction of cellulose from Horse chestnut seed shells

Seed shells of horse chestnut were gathered from Fırat University Campus (Elazığ, Turkey) and used in this study as the source of cellulose. Firstly, cellulose was extracted using our previously reported procedure (Çiçek Özkan and Güner, 2021). Briefly, the shells were separated from the seed, milled into small pieces, washed with distilled water (80 °C, four hours, fiber/water ratio: 1/10) to remove soluble parts, filtered, and dried at 60 °C in an air circulating oven. Next, the alkali-soluble components lignin and hemicellulose were removed by performing three repeated alkali treatments conducted at 80 °C for four hours, under vigorous mechanical stirring and with 5% (w/v) NaOH solution. A subsequent bleaching treatment was performed using a solution of equal parts distilled water, sodium chloride, and acetate buffer containing NaOH, glacial acetic acid, and distilled water to remove residual lignin and obtain α-cellulose. The

cellulose was extracted at least four times, and for each analysis, fresh cellulose from horse chestnut seed shell was prepared.

Composite preparation

Chitosan/cellulose (CH/CE) composite was produced using the following procedure: Chitosan was dissolved in a 5% glacial acetic acid solution, then cellulose was added to the resulting chitosan solution with continuous mechanical stirring for two hours, followed by 1-h of sonication. Chitosan/graphene (CH/G) composite was prepared by dissolving chitosan in a 5% solution of the glacial acetic acid solution and then adding graphene under mechanical stirring for two hours, followed by 1 h of sonication at room temperature according to a previously described process with slight modification (Çiçek Ozkan, 2021). The CH/G solution was prepared before adding cellulose for a homogenous chitosan-graphene suspension; next, cellulose was added and stirred to prepare the CH/CE/G composite. The crosslinked CH/CE/G/GA composites were synthesized by the dropwise addition of glutaraldehyde into the CH/CE/G mixture with 300 rpm stirring for 3 h. Next, 5 M NaOH solution was gradually added to the mixture with magnetic stirring until the solution's pH reached 7, and the formed precipitate was separated with vacuum filtration, washed with distilled water, and dried at 50 °C using the "Casting/Solvent Evaporation Method.". The same procedure was applied to prepare CH/CE/GA crosslinked composite by adding glutaraldehyde into the CH/CE suspension. The amount of components that formed the composites is presented in Table 1. Three samples of each composite were freshly prepared for individual analysis.

Characterization

Fourier transform infrared spectroscopy

FT-IR (Thermo Scientific Nicolet IS 5, USA) was used to record the spectra of samples. The tests were performed in the attenuated total reflection (ATR) mode at a resolution of 4 cm^{-1} in the wavelength range of 550–4000 cm^{-1}. The FT-IR spectrum analysis was repeated three times.

X-ray diffraction (XRD)

An X-ray diffractometer (PANalytical Empyrean, The Netherlands) with Cu Kα radiation in a 2θ range of 5°–50° was used to characterize the crystalline structure of the samples. The XRD analysis was repeated three times.

Thermal gravimetric analysis (TGA)

Thermogravimetric measurements (TA Instruments Q500) were carried out to determine the thermal stability of the samples heated at temperatures ranging from ambient temperature to 600 at a 10 °C/min heating rate under the air atmosphere. The TGA analysis was performed once by taking the sample from different points of the prepared composites.

Surface analysis

In the contact mode, the topographical analysis of samples was examined using Atomic Force Microscope (A.F.M., Park System XE15). The AFM analysis was repeated three times. The morphological investigations were performed using Field Emission Scanning Electron Microscope (FE-SEMM) (ZEISS Sigma 300). The sample surfaces were coated with a thin gold film to increase the electrical conductivity during the scanning process. The FE-SEM analysis was performed once.

Table 1 The amounts of composite components

Composite components	CH/G	CH/CE	CH/CE/G	CH/CE/GA	CH/CE/G/GA
Chitosan (g)	4	2	2	2	2
Cellulose (g)	0	2	2	2	2
Graphene (g)	0.04	0	0.04	0	0.04
Glutaraldehyde (mL)	0	0	0	1	1

Swelling behavior

The swelling properties of the two composites were investigated in three phosphate buffer solutions having pH values of 1.5, 3.5, 5.5, 7.5, and 9.5 to determine the pH sensitivity of samples by a pH meter (HANNA HI2002-02 edge). The experiment was repeated three times independently under the same conditions. Preweighed samples were immersed in the buffer solutions and measured until an equilibrium state was reached. The equilibrium swelling ratio of the composites was determined by the following Eq. (1):

$$Swellingratio(g/g) = \frac{W_S - W_D}{W_D} \times 100 \quad (1)$$

where W_S and W_D are the swollen and dry weights of composites, respectively.

^{13}C Solid-state NMR

^{13}C solid-state NMR studies were carried out using a Bruker Superconducting FT NMR Spectrometer Avance TM equipped with 4 mm Cross Polarization with magic angle spinning (CP-MAS) solids probe operating at 300 MHz. The CP-MAS spectra of samples were measured at room temperature with a spinning rate of 8.5 kHz and a recycle delay time of 4 s. The solid-state NMR analysis was performed once.

Adsorption studies

The spectrophotometric measurements for basic blue 41 (BB) were carried out using a Shimadzu UV-1800 UV–vis spectrophotometer at 610 nm. Adsorption experiments were performed by immersing 20 mg composite into a flask containing 20 mL of aqueous BB blue solution. The dye concentration was determined using the UV–vis spectrophotometer at preset time intervals during adsorption. The adsorption experiments were repeated three times independently under the same conditions.

Adsorption kinetics

The adsorption capacity of the prepared composites at time t (Q_t) and adsorption capacity at equilibrium (Q_e) was computed with Eqs. (2) and (3), respectively:

$$Q_t(mg/g) = \frac{(C_0 - C_t)V}{m} \quad (2)$$

$$Q_e(mg/g) = \frac{(C_0 - C_e)V}{m} \quad (3)$$

where C_0 (mg/L), C_t (mg/L), and C_e (mg/L) are initial, at time t, and the equilibrium concentration of BB, respectively. V (L) are the volumes of the dye solution, and m (g) is the weight of the dry composites, respectively.

Effect of initial basic blue 41 concentration and pH

The dependency of the BB adsorption process on the initial dye solution pH and concentration was investigated with the above-described method. The effect of pH was studied in adjusted dye solutions with 0.1 M NaOH and 0.1 M HCl from pH 1.5–9.5. In addition, the influence of initial BB concentration on the adsorption capacity of the produced composites was determined along with varied dye concentrations between 50–250 mg/L.

Results and discussion

Structure of composites and precursors

Figure 1 shows the comparative FTIR spectrums of the composites and their precursors. The characteristic peaks of chitosan exhibited at 3363, 3279, 2925, 2870, 1653, 1574, and 1027 cm^{-1} corresponded to O–H stretching, N–H stretching, methylene C-H stretching (CH_2), methyl C-H stretching ($–CH_3$), O–H bending (characteristic of the amide group, amide I), N–H bending (NH_2) and vibrations related to the C–O stretching (vibration of pyranose ring), respectively (Lin et al. 2015; Reghioua et al. 2021). The characteristic peaks of graphene appear at 3355, 1558, and 1066 cm^{-1}, attributed to the C–OH bonds (Aziz et al. 2014). The bands between ~ 3000 and 3500 cm^{-1} are either absent or broader, and the peak intensities are higher for CH/G composite relative to bands for chitosan, indicating the interaction between chitosan and graphene. The strong characteristic peaks of cellulose at 3331, 2904, 1629, and 1016 cm^{-1} are attributed to O–H and C–H's asymmetric and

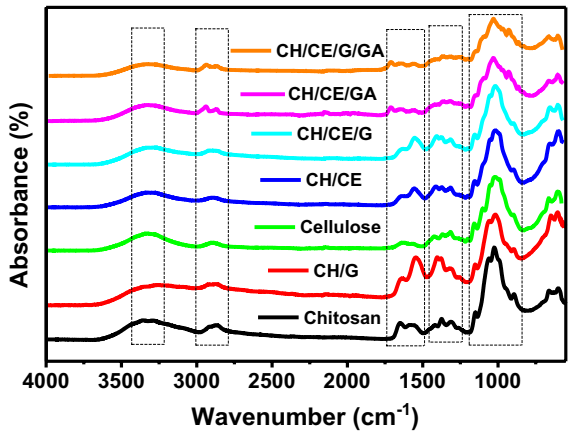

Fig. 1 FT-IR spectra of the chitosan, CH/G, cellulose, CH/CE, CH/CE/G, CH/CE/GA, and CH/CE/G/GA

symmetric stretching, O–H's bending vibration, and C–O stretching, respectively. Along with presenting similar spectrums with chitosan and cellulose, the characteristic peaks at ~ 3000–3500 cm^{-1} are missing and/or broader for non-crosslinked composites compared to similar bands for precursors. This may occur because of hydrogen bonding between N–H and O–H groups of chitosan and cellulose and their interactions with graphene. Two sharper peaks are demonstrated in the band spectrum for non-crosslinked composites between ~ 1700 and 1480 cm^{-1} and are attributed to the N–H bending. These peak intensities were drastically decreased, and a new band that appeared at ~ 1713 cm^{-1} was assigned as aldehyde vibration in the crosslinked CH/CE/GA and CH/CE/G/GA spectrum as strong evidence of the crosslinked composite formation. Other band features including several bands between ~ 800 and 1200 cm^{-1}, amide III at ~ 1370 cm^{-1}, methyl deformation at ~ 1400 cm^{-1}, and the bands between ~ 3000 and 2800 cm^{-1} support the formation of C–O–H, C–O–C, and C–N–H asymmetric stretching. These band-activity alterations may be explained by steric hindrance in polymer composite networks due to hydrogen bonding, crosslinking, and/or interactions arising among the composite components chitosan, graphene, and/or cellulose (Udoetok et al. 2016). Because of interactions and crosslinking, whereas the FTIR spectrum of crosslinked CH/CE/GA and CH/CE/G/GA shows characteristic peaks of precursors, they are sharper, absent, or broader and present lower intensity relative to similar bands for the precursors and non-crosslinked composites.

The illustrations and possible interactions of crosslinked CH/CE/GA and CH/CE/G/GA ternary Chitosan/Cellulose/Graphene composite systems seen in Fig. 2 were prepared using the "Casting/Solvent Evaporation Method."

Thermogravimetric analysis

TGA thermograms of chitosan, CH/G, cellulose, CH/CE, CH/CE/G, CH/CE/GA, and CH/CE/G/GA are shown in Fig. 3a and b to compare the thermal properties of the composites and their precursors. The first weight decrease occurred between ~24 and 120 °C for all materials indicated by evaporation of the retained moisture. Chitosan presents a single thermal decomposition stage that occurs at ~ 300 °C. The thermal degradation of cellulose was divided into 2 phases after water evaporation. The first stage was the degradation of lignocellulosic components of hemicellulose ca. ~ 242 °C, and the next was the decomposition of cellulose at ~ 327 °C. Whereas chitosan and cellulose occur in one and two thermal events, a further thermal decomposition phase was observed for chitosan, graphene, and cellulose composites,

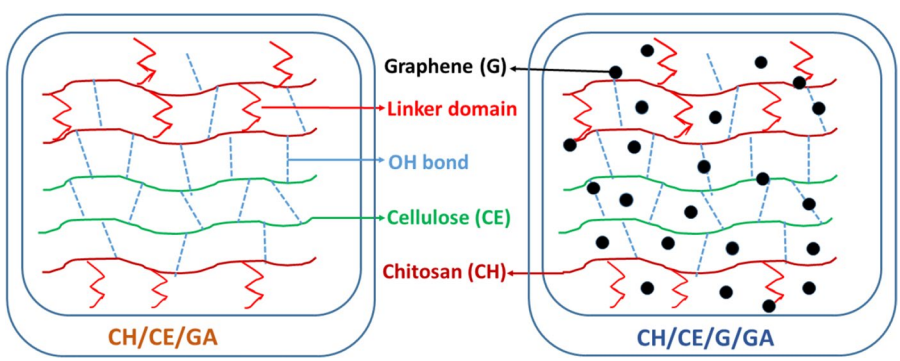

Fig. 2 Illustration of the proposed structure and possible interactions/crosslinking of **a**, **c** CH/CE/GA and **b**, **d** CH/CE/G/GA

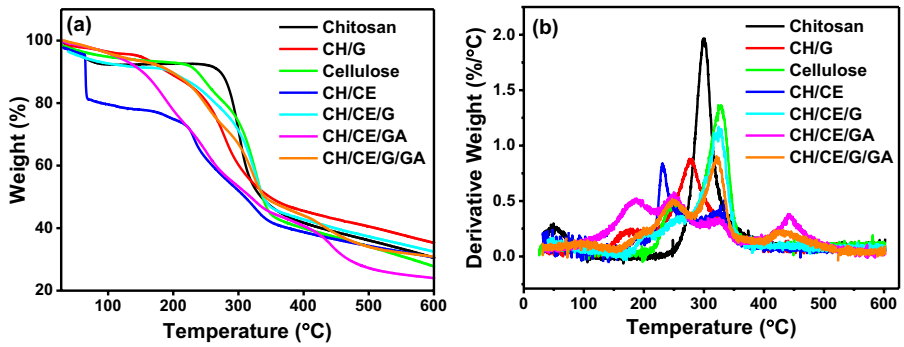

Fig. 3 TGA thermograms of cellulose, chitosan, and cellulose-graphene-chitosan-based composites

as shown in Table 2. This thermal degradation, appearing at ca. 170–200 °C without any relation to crosslinking, probably occurred due to hydrogen bonding and interactions between composite components as mentioned above for the FTIR spectrums. The thermal decompositions observed in the thermograms for CH/G, CH/CE, CH/CE/G, CH/CE/GA, CH/CE/G/GA at ~ 279 °C, ~ 231 °C, ~ 248 °C, ~ 251 °C, and ~ 250 °C corresponded to the degradation of chitosan and lignocellulosic components, respectively (Table 2). The degradation temperature at ~ 326 °C, ~ 322 °C, ~ 329 °C, and ~ 329 °C related to the decomposition of cellulose for CH/CE, CH/CE/G, CH/CE/GA, and CH/CE/G/GA composites, respectively. The cross-linked composites CH/CE/GA and CH/CE/G/GA demonstrate a fourth distinctive thermal event at 445 °C and 428 °C, corresponding to the decomposition of chitosan, graphene, cellulose, and linker domains of the materials, in agreement with a previous report (Udoetok et al. 2016). The specific surface areas of the composites were increased by graphene, which resulted in improved interaction between the polymer matrix and graphene, limited the mobility of the polymer, and hence enhanced the stability. Char residual yield for CH, CH/G, CH/CE, CH/CE/G, CH/CE/GA, and CH/CE/G/GA were 30.34%, 35.20%, 27.64%, 30.56%, 32.36%, 23.95%, and 30.78%, respectively. Accordingly, graphene-containing composites displayed higher char residue; this may have occurred due to the non-polymeric content of the composite, encouraging higher char residue formation. As affirmed by thermal analysis, the structural properties of chitosan, graphene, and cellulose are protected according to the FTIR results mentioned above. Shifting in the thermal stages of the composites relative to precursors indicates the higher thermal stability of the composite.

Crystalline conformation

XRD patterns of chitosan, cellulose, CH/G, CH/CE, CH/CE/G, CH/CE/GA, and CH/CE/G/GA are shown in Fig. 4. The characteristic diffraction peaks of chitosan were revealed at ~10° and ~20°. Cellulose extracted from horse chestnut seeds displayed a salient peak at a 2θ value of ~15° related to the crystalline structure of cellulose. The other major peak from cellulose-Iβ appeared at ~ 22°, corresponding

Table 2 Thermal properties of chitosan, CH/G, cellulose, CH/CE, CH/CE/G, CH/CE/GA, and CH/CE/G/GA

Sample	1st thermal degradation (°C)	2nd thermal degradation (°C)	3rd thermal degradation (°C)	4th thermal degradation (°C)	Char residual (%)
Chitosan	300	–	–	–	30.34
CH/G	173	279	–	–	35.20
Cellulose	242	327	–	–	27.64
CH/CE	191	231	326	–	30.56
CH/CE/G	199	248	322	–	32.36
CH/CE/GA	184	251	329	445	23.95
CH/CE/G/GA	194	250	322	428	30.78

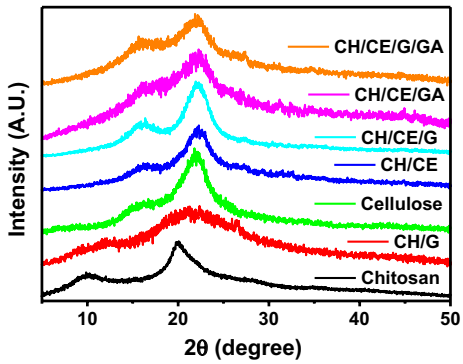

Fig. 4 X-Ray patterns of the chitosan, cellulose, CH/G, CH/CE, CH/CE/G, CH/CE/GA, and CH/CE/G/GA

to the plane (200). The peak at 22° in the crystalline polymorph structure of pure cellulose is typical for cellulose I, consistent with the previously reported study by Yang et al. (2016b). The X-ray diffraction diagram for graphene powder demonstrates a broader peak structured between the crystalline and amorphous related to the plane (002) at 26.5°, as reported in a previous report (Siburian et al. 2018). XRD lines of CH/G composite present two broader peaks at ~ 12° and ~ 21.5°, which may originate from interactions between chitosan and graphene in agreement with FTIR and TGA results. The CH/CE composite recorded two peaks at 16.2° and 22°, while the CH/CE/G composite displayed the XRD peaks at 16.3° and 22.3°. The graphene peak in CH/G and CH/CE/G disappeared, which may have resulted from the exfoliation of graphene sheets as a result of the ultrasonication step or due to the small content of graphene sheets compared to the polymer content (only 1%) in agreement with the previous report (Hegazy and Mohamed, 2021).

The XRD patterns of bio-nano composites imply the preservation of the essential structural characteristics of precursors. However, the crystallinity of CH/CE/G is higher relative to CH/CE due to the presence of graphene. The non-crosslinked CH/CE and CH/CE/G present sharper peaks compared to crosslinked CH/CCE/GA and CH/CE/G/GA composites, which might be related to increasing crystallinity because of hydrogen bonding, the intra-, and intermolecular interactions, and crosslinking between chitosan, graphene, and cellulose. Furthermore, increasing GA content decreases crystallinity because of the crosslinking reported by Udoetok et al. (2016). The diffraction peaks were detected at 2θ degrees of CH/CE/GA (18° and 22.3°) and CH/CE/G/GA (16.7° and 22.2°), indicating the new arrangement of cellulose and chitosan in the bio-nano composites due to the crosslinking.

^{13}C Solid-state NMR spectroscopy

The ^{13}C CP-MAS-NMR spectra for chitosan, cellulose, CH/CE, CH/CE/G, and crosslinked CH/CE/G/GA composite are demonstrated in Fig. 5. The NMR spectra of chitosan powder demonstrate ^{13}C bands for C1 (103.1 ppm), C2 (55.3 ppm), C3,5 (73.3 ppm), C4 (80.5 ppm), C6 (59.1 ppm), C=O (171.9 ppm), and CH_3 (21.7 ppm). The produced cellulose displays a chemical shift at 103.1 nm for C1, 70.5 nm for C2, 73.1 ppm for C3, C5, 86.8/82.0 ppm for C4, and 62.9/60.8 ppm for C6. Compared with cellulose, chitosan has a distinctly different NMR spectrum seen at bands corresponding to C4 and C6, where chitosan presents a single band, cellulose shows a doublet band, in agreement with previous reports (Tran et al. 2013; Udoetok et al. 2016). The resonance line for C2 in the cellulose spectrum stands with C3,5 in a large band, whereas chitosan shows a single band at 73.3 ppm only for C3,5 and C2 and C6 in a wide doublet band. However, the bands related to C=O at 171.8 ppm and the CH_3 group at 21.7 ppm in the resonance line for chitosan are associated with carbonyl and methyl groups of monomeric chitin, respectively, which appear due to incomplete deacetylation

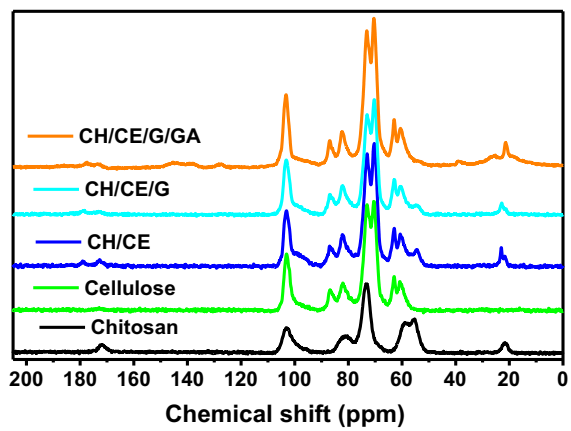

Fig. 5 ^{13}C CP-MAS solid NMR spectra of chitosan, cellulose, CH/CE, CH/CE/G, and CH/CE/G/GA

of chitin in commercial chitosan (80% deacetylation degree). The produced composites demonstrate similar ^{13}C NMR spectrum bands with the precursors' chitosan and cellulose, attributing to the preserved fundamental structure of unmodified biopolymers and successfully regenerating composites as agreed with the FTIR, TGA, and XRD results above. A chemical shift at 179.1 ppm was strikingly observed in ^{13}C spectra of CH/CE and CH/CE/G composites differently from chitosan and cellulose spectra, which might be related to an imine bond formation between chitosan amine and chitin carbonyl groups due to protonation in the acetic acid medium. The spectral difference of the CH/CE composite compared to the CH/CE/G composite with only a single band at 22.8 ppm appears with a doublet CH_3 band at 23.0 ppm and 21.7 ppm, which might be related to two chemical environments (Toeri et al. 2017). The ^{13}C NMR spectrum of crosslinked CH/CE/G/GA composite has a different spectrum compared to the chitosan, cellulose, non-crosslinked CH/CE/G, and CH/CE composite. The band shift variations related to the crosslinked CH/CE/G/GA, arising new spectral bands at 25.2/39.1 ppm and 128.2–145.5/137.7 ppm, which are associated with methylene groups of GA with the distinct chemical environments, and conjugated ethylenic bond, in agreement with other reports (Toeri et al. 2017; Zhang et al. 2019).

Morphological properties

The surface morphology of cellulose, CH/CE/G, and CH/CE/G/GA was investigated using scanning electron microscopy (SEM), as presented in Fig. 6a–c, respectively. The discrete sheet or film-like structure of G and the banded structure of chitosan associated with its tendency to self-aggregation have been shown in previous reports (Muthuchamy et al. 2020; Yan and Chen, 2011). The morphology of cellulose produced from horse chestnut seed shells, displayed in Fig. 6a-1, 2, reveals a homogeneous structure and dense bundle of fibers. On the other hand, the large and dense fibrous structure of cellulose and banded sheet/film-like morphology of chitosan and graphene, as shown in Fig. 6b-1, 2, indicates a good interaction and integration with non-crosslinked CH/CE/G composite. CH/CE/G/GA exhibited an entirely different structure relative to non-crosslinked CH/CE/G because of intra- and intermolecular cross-linking reactions, which caused the morphological change in the cross-linked composite (Fig. 6c-1, 2). Furthermore, the crosslinker content in the composite material causes alteration in structure, morphology, roughness, and porosity, as determined in related reports (Udoetok et al. 2016; Yan and Chen, 2011; Zhao et al. 2019). In addition, a minimal amount of graphene leads to significant changes in the morphology of bionano composite materials (Rodríguez-González et al. 2020).

Surface topography

The surface characteristic, morphology, and topography of materials significantly influence their material properties, such as hydrophobicity for various application areas. The topographic investigation of cellulose, CH/CE/G, and CH/CE/G/GA was performed on a glass substrate illustrated by AFM and shown in Fig. 7a–c, respectively. While cellulose exhibited a smooth surface morphology, the rough topographic feature of the CH/CE/G composites increased by incorporating graphene into the composite structure, as reported in the literature [7]. The root means square (RMS or Rq) roughness values for cellulose, CH/CE/G, and CH/CE/G/GA were calculated to be 551, 347, and 654 nm, respectively, for 100 μm^2 area at various points on the films. The relatively higher value of Rq may have originated from a densely packed structure resulting from the intra- and intermolecular cross-linking reaction of chitosan via glutaraldehyde for CH/CE/G/GA. On the other hand, CH/CE/G had an interestingly low roughness value than cellulose and CH/CE/ G/GA.

Swelling properties of composites

The molecular structure change of the prepared composites relative to the precursors led to various physical properties, which can be determined using techniques such as thermal analysis, crystallinity, FT-IR spectroscopy, swelling, and morphological studies. The equilibrium swelling behavior of CH/CE, CH/CE/G, CH/CE/GA, and CH/CE/G/GA were investigated in five phosphate-buffered saline solutions with pH 1.5, 3.5, 5.5, 7.5, and 9.5 at room temperature as shown in Fig. 8a. The experiment was repeated three times independently under the same conditions, and the results were averaged to determine the statistical

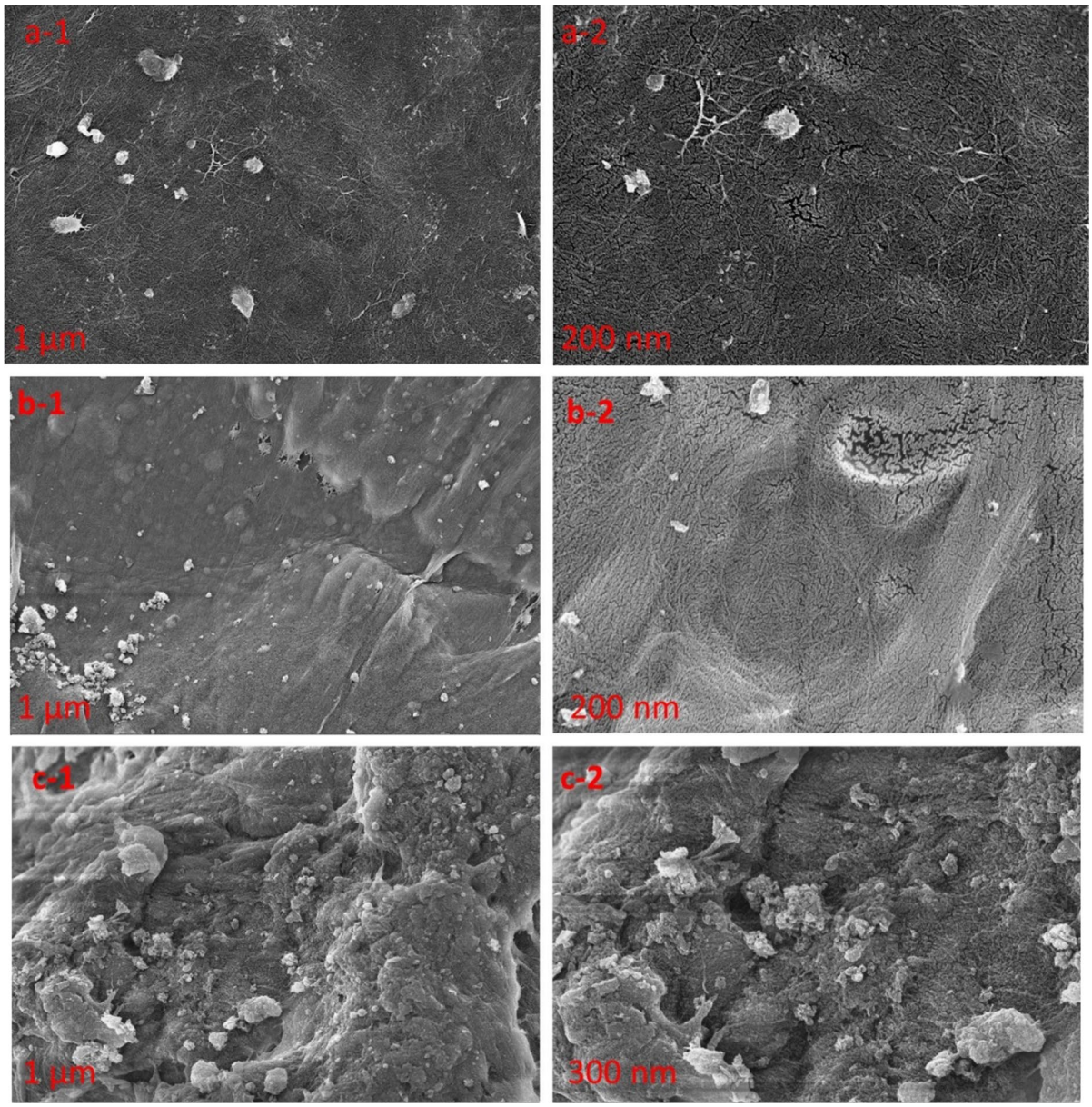

Fig. 6 SEM micrographs of cellulose **a-1** and **a-2**, CH/CE/G **b-1** and **b-2**, and CH/CE/G/GA **c-1** and **c-2**

deviations shown with error bars. It was figured out that all non-crosslinked (CH/CE and CH/CE/G) and crosslinked (CH/CE/GA and CH/CCE/G/GA) composites presented similar swelling ratio dependency to the pH values. The equilibrium swelling ratio of non-crosslinked CH/CE and CH/CE/G in various pHs was higher relative to crosslinked CH/CE/GA and CH/CE/G/GA, along with significantly decreased within the pH 5.5–9.5 and increased within 1.5–5.5 demonstrating the maximum swelling capacity at pH 5.5. The swelling ratios of crosslinked and non-crosslinked bio-nano composite increased with decreasing pH, consistent with the amino groups of chitosan, which was ionized and protonated in the form of NH_3^+, resulting in an expansion of the composite network and penetration of more water into the polymer matrix, in agreement with previous reports (Karimi et al. 2017; Rasoulzadehzali and Namazi,

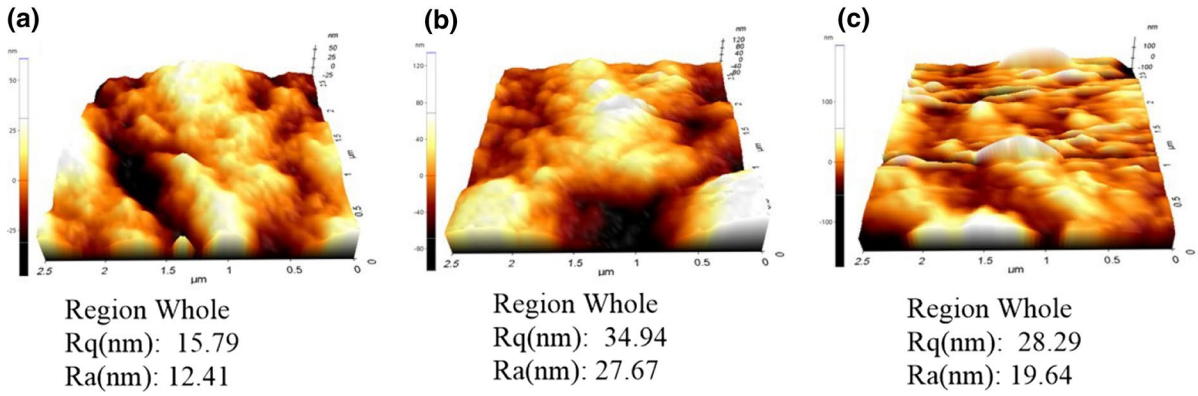

Fig. 7 AFM topographic images of **a** Cellulose, **b** CH/CE/G, and **c** CH/CE/G/GA

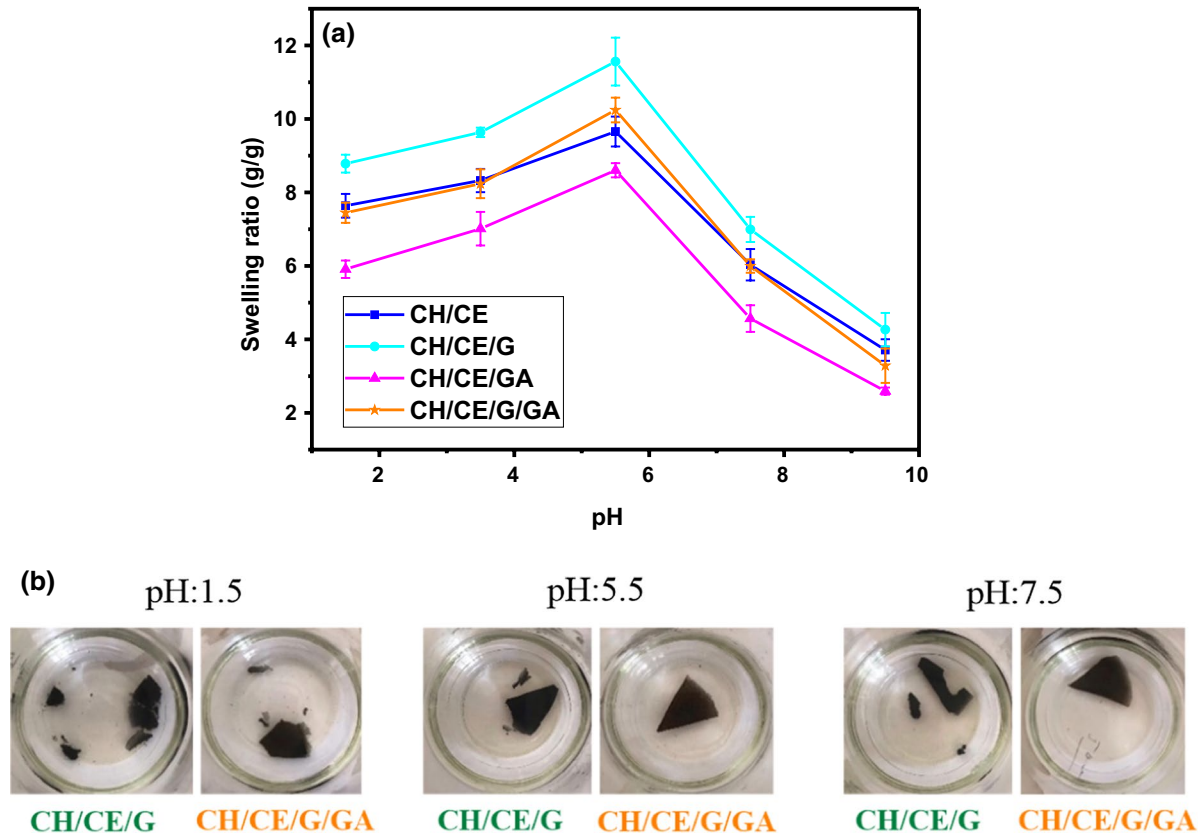

Fig. 8 **a** The effect of pH on the swelling behaviors of CH/CE/G and CH/C/G/GA composites, **b** The images of CH/CE/G and CH/CE/G/GA composites at pH 1.5, 5.5, and 7.5 (by immersing the samples during 72 h in 0.10 M phosphate-buffered solution at room temperature)

2018; Wang et al. 2017). However, chitosan and cellulose are semi-crystalline materials with crystalline and amorphous areas, and the amorphous part of cellulose contains a high ratio of OH groups, promoting the liquid absorption capacity of the composites. Furthermore, introducing graphene into the CH/CE/G

composite network can increase swelling capacity in solutions with different pH values. The swelling studies approve the pH-dependent swelling behaviors of prepared composites.

The interactions between chitosan, cellulose, and graphene and crosslinking reaction play a vital role in the adsorption process of the crosslinked composites as follows: (i) The integrity and strength of the composite network are impressed by cross-linking degree; (ii) It hinders dissolution and (iii) It decreases hygroscopicity and swelling ratio of the composite (Mokhothu and John, 2015). The cross-linking reaction produces a network with fewer numbers of free NH_2 groups available for protonation and subsequent swelling in acidic media. This leads to a decrease or loss in the swelling ratio of the cross-linked composite at all pH values (Çiçek Ozkan, 2021; Wang et al. 2017). Therefore, the integrity of composites can be preserved through the crosslinking reaction as demonstrated in Fig. 8b at the equilibrium swelling state and pH 1.5, 5.5, and 7.5 for CH/CE/G and CH/CE/G/GA bio-nano composites. The cross-linking degree corresponding to the glutaraldehyde amount can also affect the swelling ratio of composites, as reported in our previous study (Çiçek Ozkan, 2021).

Stability in aqueous media

The stability of the prepared composites was investigated in distilled water medium at room temperature. The water uptake ratios of the prepared composites in 24 h are listed in Table 3. The non-crosslinked composites CH/CE and CH/CE/G demonstrated higher swelling capacity in water relative to the crosslinked composites CH/CE/GA and CH/CE/G/GA due to the decreasing ratio of hydrophilic groups after cross-linking. The CH/CE/G composite reinforced with graphene gained excellent stability in an aqueous medium compared to the CH/CE. The CH/CE composite began to lose integrity after 24 h and entirely broke into pieces after 5 days in water media, whereas the CH/CE/G composite started breaking down after 5 days (Fig. 9a,b). The stability of CH/CE/GA and CH/CE/G/GA composites was enhanced via crosslinking by glutaraldehyde in the aqueous medium compared to the non-crosslinked composites. As shown in Fig. 9c,d, tiny lacerations were observed on the edges of CH/CE/GA, whereas the graphene-reinforced CH/CE/G/GA preserved the integrity after swelling in the aqueous medium for 5 days.

Table 3 The water uptake ratios of prepared composites

Sample	Water uptake ratio (g/g)
CH/CE	11.69 ± 0,34
CH/CE/G	12.13 ± 0,51
CH/CE/GA	5.85 ± 0,74
CH/CE/G/GA	6.81 ± 0,49

Adsorption of basic blue 41

Adsorption kinetics

The dye adsorption process corresponding to the adsorption rate, mechanism, and steps of the produced composites can be described by applying adsorption kinetics. The adsorption behaviors of the crosslinked CH/CE/GA and CH/CE/G/GA composites for BB at 25, 35, and 45 °C are demonstrated in Fig. 10a–c, respectively. The composites present a rapid adsorption increase at the beginning of the process, and then the adsorption rate slows down and reaches equilibrium; this may have originated from the presence of comprehensive free sites for adsorption and higher BB concentration at the initial stage (Dai et al. 2018). As shown in Fig. 10a–c, the adsorption ability of the produced composites increased from 25 to 35 °C and then decreased from 35 to 45 °C. The decrease in the adsorption ability of the composites at 45 °C can be explained by an increase in the large BB dye ion movability during the adsorption process, causing a decrease in adsorption ability in agreement with previous reports (Özer et al. 2007; Wang et al. 2008). The equilibrium swelling capacity of CH/CE/GA was 82.39, 85.64, and 82.56 mg/g at 25, 35, and 45 °C, respectively. After introducing graphene, CH/CE/G/GA composite showed higher adsorption ability with 90.67, 99.46, and 93.19 mg/g at 25, 35, and 45 °C, respectively.

The BB dye adsorption process of the prepared composites was investigated at 25, 35, and 45 °C using pseudo-first-order [Eq. (4)] and pseudo-second-order [(Eq. (5)] kinetic models.

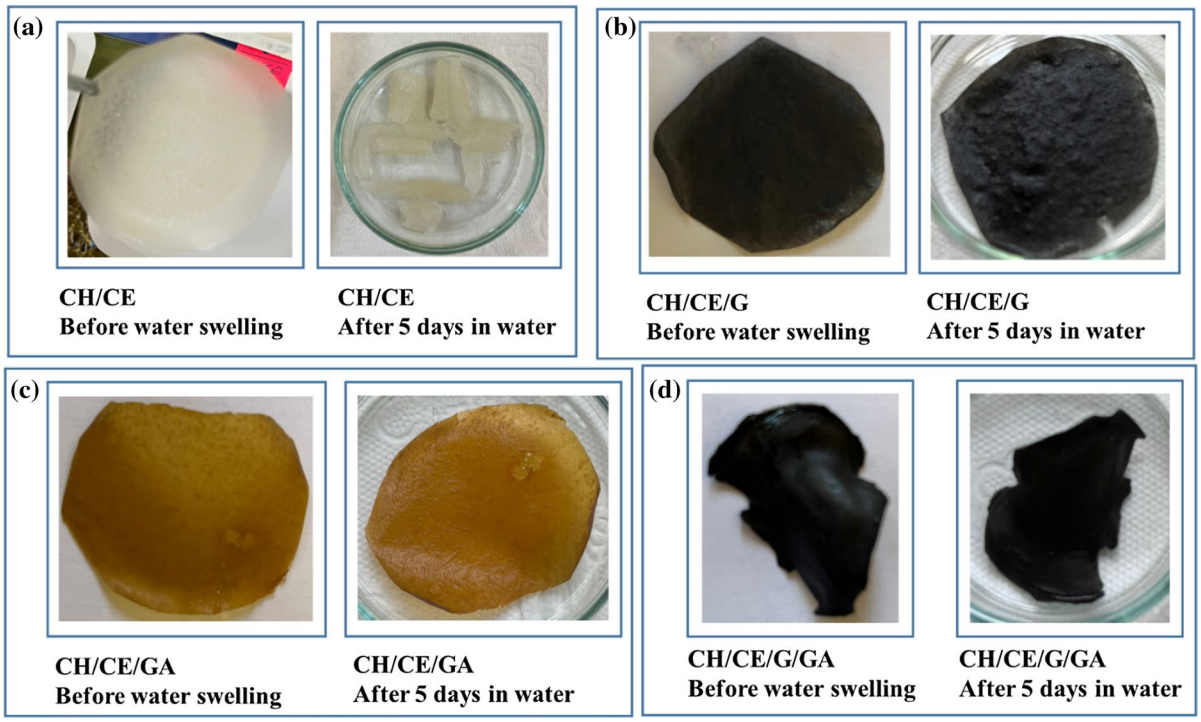

Fig. 9 The photo of **a** CH/CE, **b** CH/CE/G, **c** CH/CE/GA, and **c** CH/CE/G/GA composites before and after swelling in aqueous media

$$Log\left(Q_e - Q_t\right) = LogQ_e - \frac{k_1}{2.303}t \tag{4}$$

$$\frac{t}{Q_t} = \frac{1}{k_2 Q_e^2} + \frac{1}{Q_e}t \tag{5}$$

where Q_e (mg/g) and Q_t (mg/g) are the BB adsorption ability of the produced composites at equilibrium and time t (min), respectively, and k_1 (min^{-1}) and k_2 (mg/g min^{-1}) are rate constants of pseudo-first-order and pseudo-second-order adsorption kinetic model, respectively. The linearized forms for pseudo-first-order and pseudo-second-order equations were shown in Figs. 10d–f and g–i at 25, 35, and 45 °C, respectively, where the parameters k_1, k_2, and theoretical equilibrium adsorption capacity ($Q_{e,\,cal}$) for two models were obtained. The parameters for kinetic models and experimental equilibrium adsorption capacity ($Q_{e,\,exp}$) at 25, 35, and 45 °C were listed and compared in Table 4. It was figured out that the correlation coefficients (R^2) for pseudo-second-order kinetics obtained at different temperatures were higher than R^2 for the pseudo-first-order model. However, by the pseudo-first-order kinetic model, the kinetic parameters could be linearized up to the time 140 min, 80 min, and 120 min at 25, 35, and 45 °C, respectively. In contrast, the pseudo-second-order kinetic equation can be fitted up to 250 min, which is more consistent with the adsorption kinetics of the used composites. The results indicate that the pseudo-second-order model better correlates BB adsorption onto the prepared composites. In addition, the theoretical $Q_{e,\,cal}$ values from the pseudo-second-order model better fit with $Q_{e,\,exp}$ amounts of adsorbed BB, attributes further approving of influence of this model.

Reusability of prepared composites and effect of initial dye concentration and pH

The BB-loaded composites were stirred in 25 mL of 0.1 M HCl solution for 4 h at ambient temperature to provide desorption of the adsorbed dye. After desorption, the composites were washed with distilled water, and the previously used adsorption process was performed with the fresh dye solution. Unfortunately, the

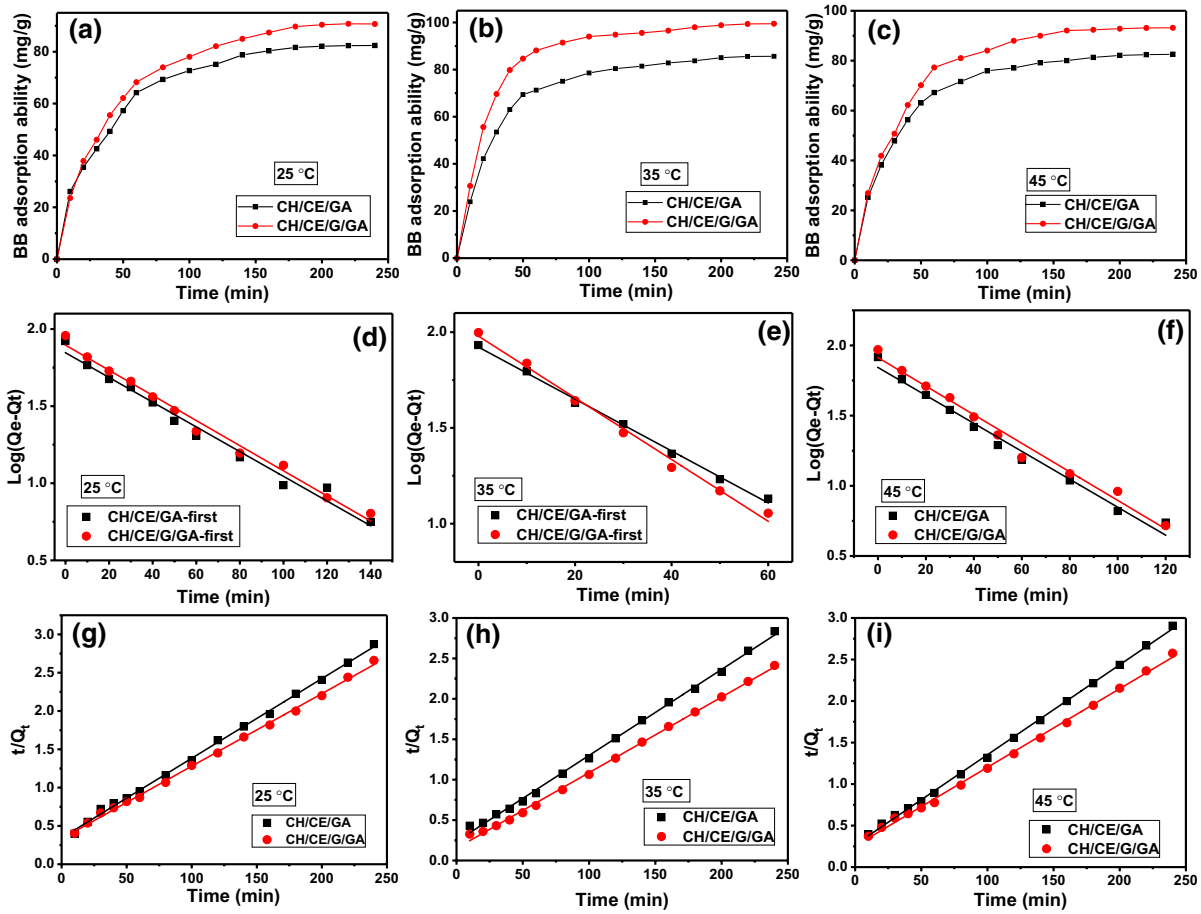

Fig. 10 Adsorption ability of CH/CE/GA and CH/CE/G/GA for BB at 25 °C (**a**), 35 °C (**b**), and 45 °C (**c**); pseudo-first-order kinetic (**d**–**f**) and pseudo-second-order kinetic (**g**–**i**) of BB at 25, 35, and 45 °C

Table 4 Comparison of pseudo-first and -second-order kinetic models parameter for BB adsorption onto the prepared crosslinked composites

Composites	Q_e (mg/g)	Pseudo-first-order kinetic			Pseudo-second-order kinetic		
		R^2	$Q_{e\text{-}1}$ (mg/g)	k_1 (min^{-1})	R^2	$Q_{e\text{-}2}$ (mg/g)	k_2 ($mg/gmin^{-1}$)
25 °C							
CH/CE/GA	82.39	0.9826	70.19	0.0185	0.9984	96.15	3.15×10^{-4}
CH/CE/G/GA	90.67	0.9892	78.65	0.0188	0.9983	96.43	3.22×10^{-4}
35 °C							
CH/CE/GA	85.64	0.9972	83.57	0.0312	0.9981	93.98	4.79×10^{-4}
CH/CE/G/GA	99.46	0.9933	95.33	0.0371	0.9985	106.95	5.75×10^{-4}
45 °C							
CH/CE/GA	82.56	0.9844	69.68	0.0229	0.9992	92.25	4.36×10^{-4}
CH/CE/G/GA	93.19	0.9857	81.90	0.0234	0.9982	98.23	4.07×10^{-4}

prepared CH/CE/GA and CH/CE/G/GA composites lost approximately half of their adsorption efficiency.

The effect of initial BB concentration varying between 50 and 250 mg/L on the adsorption ability of CH/CE/GA and CH/CE/G/GA composites was studied at 25 °C. The experiment was repeated three times independently under the same conditions. The experimental results were averaged and the statistical deviations were expressed as error bars as shown in Fig. 11a and b. The equilibrium adsorption capacities of the composites increased with the initial BB concentration, indicating a driving force generated to cope with mass transfer resistance (Özer et al. 2007). The increasing trend in the adsorption capacity of the composites with increasing initial BB concentration may also be due to the interactions between dye and composites (Afshin et al. 2018). The increase in initial BB concentration achieves a saturation state after 200 mg/L for the CH/CE/GA composite, whereas it keeps increasing for the CH/CE/G/GA composite.

Along with the increasing concentration of BB from 50 to 250 mg/L, the adsorption capacity of CH/CE/GA and CH/CE/G/GA improves from 41.84 to 104.51 mg/g and from 44.10 to 121.28 mg/g, respectively. The saturation tendency for BB adsorption at higher concentrations arises from a limited number of binding sites on the composites. However, the higher surface area obtained by introducing graphene further increases the adsorption ability of the CH/CE/G/GA composite relative to CH/CE/GA (Liu et al. 2012).

Figure 11b demonstrates the adsorption capacities of CH/CE/GA and CH/CE/G/GA composites at 25 °C for various pH values. The acidity of the dye solution is an essential parameter for the adsorption process because it influences the surface charge density of composites and dissociates the functional groups on the active sites of adsorbents, thereby affecting the adsorption performance (H. Yang et al. 2016a, b). The adsorption capacity of composites presents similar trends at pH values between 1.5 and 9.5, which increase gradually from 1.5 to 5.5, then achieve a slightly growing plateau. The composites' surfaces become positively charged owing to the protonation of –OH and –NH groups at lower pH values, resulting in H^+ ions engagement with dye cations and reducing the adsorption capacity through the electrostatic repulsion force (Bhattacharya and Sharma, 2005; Bulut and Aydin, 2006; Firdaus et al. 2021). Similar results were also obtained by Ali et al. in a study performed on acid blue and basic blue dye adsorption onto activated charcoal (2020).

Adsorption İsotherm

The adsorption capacities of different adsorbents and their adsorption properties for various dyes and pollutants can be comparatively investigated by adsorption isotherms. The adsorption capacity of the adsorbent can be explained with equilibrium studies. The surface adsorption properties and affinity can be demonstrated using constants that characterize the adsorption isotherms. The most widely used "Freundlich and Langmuir" isotherm models were applied to design adsorption systems and define isotherm parameters for BB adsorption onto the produced composites. The linear forms of Freundlich [Eq. (6)] and Langmuir [Eq. (7)] models are given as

$$lnQ_e = lnK_F + \frac{1}{n} lnC_e \tag{6}$$

$$\frac{C_e}{Q_e} = \frac{C_e}{Q_{max}} + \frac{I}{K_L Q_{max}} \tag{7}$$

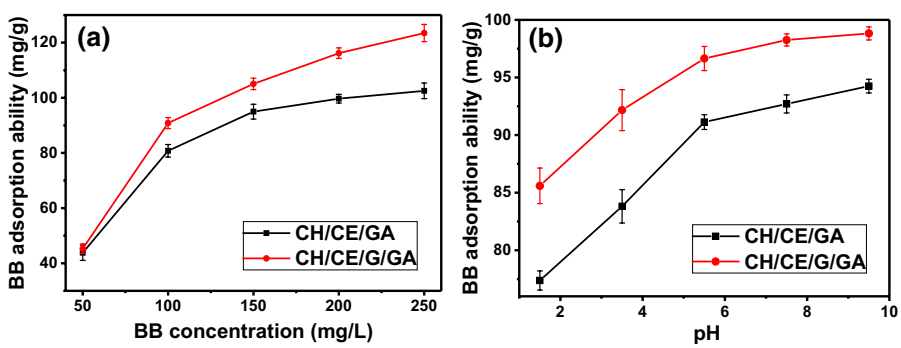

Fig. 11 The equilibrium adsorption capacity of CH/CE/GA and CH/CE/G/GA **a** at different initial BB concentrations, **b** at different pHs

Table 5 The Langmuir and Freundlich model parameters for BB adsorption onto the prepared composites

Composites	Langmuir model			Freundlich model		
	Q_{max} (mg g^{-1})	K_L (L mg^{-1})	R^2	K_F (mg g^{-1})	*n*	R^2
CH/CE/GA	107.87	0.1284	0.9996	31.82	3.93	0.8617
CH/CE/G/GA	129.3	0.1326	0.9964	38.86	3.97	0.7783

where Q_e (mg/g) is adsorption capacity at equilibrium, C_e is equilibrium BB concentration, n is adsorption intensity, and Q_{max} is the maximal adsorption capacity. K_F [(mg/g)(L/mg)$^{1/n}$] is the Freundlich constant that indicates adsorption capacity, and K_L (L/mg) is the equilibrium adsorption constant by the Langmuir model, respectively. The adsorption isotherm constants and correlation coefficients for Langmuir and Freundlich models were calculated based on the data from Fig. 10a and listed in Table 5. The Langmuir isotherm model expressed as the monolayer adsorption based on the same energy of adsorbent active cites presents a better fit considering the R^2 values shown in Table 5 for BB adsorption onto the prepared composites. The maximum adsorption capacities of CH/CE/GA and CHE/CE/G/GA were determined as 107.87 and 129.3 mg/g, respectively, calculated from the Langmuir isotherm equation.

Conclusions

Crosslinked chitosan/cellulose/graphene composite materials were produced with alterable morphology and surface properties because of the interaction between nano-biopolymers components at changing level crosslinking and self-assembly. The cross-linking of nano-biocomposite was confirmed by FTIR and ^{13}C NMR studies. The imine bond formation was verified via FTIR at ~ 1713 cm^{-1} and 13C NMR at 179.1 ppm spectrum, whereas the interactions between chitosan, cellulose, and graphene that altered the crystallinity and thermal properties produced composites as supported by XRD and thermal analysis results. Due to graphene and crosslinking, SEM, AFM, and water uptake studies revealed a greater surface area and various morphological and topological surface properties. However, the pH sensitivity and increasing swelling ratio of fabricated composites also supported the effect of graphene presence. The adsorption studies demonstrated that the BB adsorption capacity of the prepared composites was significantly affected by the initial BB concentration, pH, and temperature. An enhanced adsorption capacity of BB was revealed for the graphene-filled composite. The Pseudo second-order kinetic and Langmuir isotherm models best defined the kinetic parameters and adsorption equilibrium. In summary, this work offers a better insight into structural and synergic effects on the adsorption properties of chitosan/ graphene/cellulose composite systems that have the potential to be utilized in water treatment, drug delivery, and skin tissue engineering.

Acknowledgments Melek Güner is acknowledged for her expert technical assistance with XRD analysis.

Funding This work was supported by Firat University Scientific Research Projects Unit (Project No.: TEKF.21.06).

Declarations

Conflict of interest The author declares that they have no known competing financial interests or personal relationships that could have influenced the work reported in this paper.

References

Abdul Khalil HPS, Saurabh CK, Adnan AS, Nurul Fazita MR, Syakir MI, Davoudpour Y, Rafatullah M, Abdullah CK, Haafiz MKMM, Dungani RS, Saurabh CK, Adnan AS, Fazita MRN, Syakir MI, Davoudpour Y, Rafatullah M, Abdullah CK, Haafiz MKMM, Dungani R (2016) A review on chitosan-cellulose blends and nanocellulose reinforced chitosan biocomposites : Properties and their applications. Carbohydr Polym 150:216–226. https://doi.org/10.1016/j.carbpol.2016.05.028

Afshin S, Mokhtari SA, Vosoughi M, Sadeghi H, Rashtbari Y (2018) Data of adsorption of Basic Blue 41 dye from aqueous solutions by activated carbon prepared from filamentous algae. Data Br 21:1008–1013. https://doi.org/10.1016/j.dib.2018.10.023

Aguirre-chagala YE, Pavón-pérez LB, Altuzar V, Domínguez-chávez JG, Muñoz-aguirre S, Mendoza-Barrera C (2017) Comparative study of one-step cross-linked electrospun chitosan-based membranes. J Nanomater 2017:1980714. https://doi.org/10.1155/2017/1980714

Alavi M, Nokhodchi A (2020) An overview on antimicrobial and wound healing properties of ZnO nanobiofilms,

hydrogels, and bionanocomposites based on cellulose, chitosan, and alginate polymers. Carbohydr Polym 227:115349. https://doi.org/10.1016/j.carbpol.2019.115349

Ali F, Ali N, Bibi I, Said A, Nawaz S, Ali Z, Salman SM, Iqbal HMN, Bilal M (2020) Adsorption isotherm, kinetics and thermodynamic of acid blue and basic blue dyes onto activated charcoal. Case Stud Chem Environ Eng 2:1–6. https://doi.org/10.1016/j.cscee.2020.100040

Askeland DR, Fulay PP, Wright WJ (2011) The science and engineering of materials, 6th edn. Cengage Learning, Stamford

Azarniya A, Eslahi N, Mahmoudi N, Simchi A (2016) Effect of graphene oxide nanosheets on the physico-mechanical properties of chitosan/bacterial cellulose nanofibrous composites. Compos Part A Appl Sci Manuf 85:113–122. https://doi.org/10.1016/j.compositesa.2016.03.011

Aziz M, Halim FSA, Jaafar J (2014) Preparation and characterization of graphene membrane electrode assembly. J Teknol Sci Eng 69:11–14. https://doi.org/10.11113/jt.v69.3388

Bhattacharya KG, Sharma A (2005) Kinetics and thermodynamics of methylene blue adsorption on Neem (Azadirachta indica) leaf powder. Dye Pigment 65:51–59. https://doi.org/10.1016/j.dyepig.2004.06.016

Bianco Prevot A, Fabbri D, Pramauro E, Baiocchi C, Medana C (2008) High-performance liquid chromatography coupled to ultraviolet diode array detection and electrospray ionization mass spectrometry for the analysis of intermediates produced in the initial steps of the photocatalytic degradation of sulfonated azo dyes. J Chromatogr A 1202:145–154. https://doi.org/10.1016/j.chroma.2008.06.038

Bodur S, Erarpat S, Bakırdere S (2020) Fe3O4/reduced graphene oxide nanocomposites based dispersive solid phase microextraction for trace determination of profenofos in white rice flour samples. J Food Compos Anal. https://doi.org/10.1016/j.jfca.2020.103516

Bulut Y, Aydin H (2006) A kinetics and thermodynamics study of methylene blue adsorption on wheat shells. Desalination 194:259–267. https://doi.org/10.1016/j.desal.2005.10.032

Butola BS, Kumar A (2020) Green chemistry based in-situ synthesis of silver nanoparticles for multifunctional finishing of chitosan polysaccharide modified cellulosic textile substrate. Int J Biol Macromol 152:1135–1145. https://doi.org/10.1016/j.ijbiomac.2019.10.202

Chen P, Xie F, Tang F, McNally T (2020) Glycerol plasticisation of chitosan/carboxymethyl cellulose composites: Role of interactions in determining structure and properties. Int J Biol Macromol 163:683–693. https://doi.org/10.1016/j.ijbiomac.2020.07.004

Çiçek Ozkan B (2021) Çapraz bağli kitosan selüloz grafen kompozitinin şişme davranişlarinin incelenmesi. Fırat Üniversitesi Mühendislik Bilim Derg 33:329–337. https://doi.org/10.35234/fumbd.858462

Çiçek Özkan B, Güner M (2021) Ultrasonik destekli asit hidrolizi ile nanokristalin selüloz üretimi. Int J Innov Eng Appl 5:101–106. https://doi.org/10.46460/ijiea.946875

Çiçek Özkan B, Güner M (2022) Isolation, characterization, and comparison of nanocrystalline cellulose from solid wastes of horse chestnut and chestnut seed shell. Cellulose. https://doi.org/10.1007/s10570-022-04682-8

Dai H, Huang Y, Huang H (2018) Eco-friendly polyvinyl alcohol/carboxymethyl cellulose hydrogels reinforced with graphene oxide and bentonite for enhanced adsorption of methylene blue. Carbohydr Polym 185:1–11. https://doi.org/10.1016/j.carbpol.2017.12.073

Demitri C, De Benedictis VM, Madaghiele M, Corcione CE, Maffezzoli A (2016) Nanostructured active chitosan-based films for food packaging applications: effect of graphene stacks on mechanical properties. Measurement 90:418–423. https://doi.org/10.1016/j.measurement.2016.05.012

Firdaus M, Yusop M, Azmier M, Ayshah N (2021) Adsorption of cationic methylene blue dye using microwave-assisted activated carbon derived from acacia wood : optimization and batch studies. Arab J Chem 14:103122. https://doi.org/10.1016/j.arabjc.2021.103122

González-López ME, Laureano-Anzaldo CM, Pérez-Fonseca AA, Gómez C, Robledo-Ortíz JR (2021) Congo red adsorption with cellulose-graphene nanoplatelets beads by differential column batch reactor. J Environ Chem Eng. https://doi.org/10.1016/j.jece.2021.105029

Harkins AL, Duri S, Kloth LC, Tran CD (2014) Chitosan-cellulose composite for wound dressing material. Part 2. Antimicrobial activity, blood absorption ability, and biocompatibility. J. Biomed Mater Res Part B Appl Biomater 102:1199–1206. https://doi.org/10.1002/jbm.b.33103

Hassanein A, Salahuddin N, Matsuda A, Kawamura G, Elfiky M (2017) Fabrication of biosensor based on Chitosan-ZnO/Polypyrrole nanocomposite modified carbon paste electrode for electroanalytical application. Mater Sci Eng C 80:494–501. https://doi.org/10.1016/j.msec.2017.04.101

Hegazy SH, Mohamed SK (2021) Starch-graft-polyacrylamide copolymer /Fe3O4 /graphene oxide nanocomposite: synthesis, characterization, and application as a low-cost adsorbent for Ni (II) from aqueous solutions. J Polym Res 28:1–14. https://doi.org/10.1007/s10965-020-02275-2

Huang T, Shao YW, Zhang Q, Deng YF, Liang ZX, Guo FZ, Li PC, Wang Y (2019) Chitosan-cross-linked graphene oxide/carboxymethyl cellulose aerogel globules with high structure stability in liquid and extremely high adsorption ability. ACS Sustain Chem Eng 7:8775–8788. https://doi.org/10.1021/acssuschemeng.9b00691

Islam MM, Shahruzzaman M, Biswas S, Nurus Sakib M, Rashid TU (2020) Chitosan based bioactive materials in tissue engineering applications-a review. Bioact Mater 5:164–183. https://doi.org/10.1016/j.bioactmat.2020.01.012

Jawad AH, Norrahma SSA, Hameed BH, Ismail K (2019) Chitosan-glyoxal film as a superior adsorbent for two structurally different reactive and acid dyes: adsorption and mechanism study. Int J Biol Macromol 135:569–581. https://doi.org/10.1016/j.ijbiomac.2019.05.127

Jawad AH, Abdulhameed AS, Malek NNA, Al-Othman ZA (2020) Statistical optimization and modeling for color removal and COD reduction of reactive blue 19 dye by mesoporous chitosan-epichlorohydrin/kaolin clay composite. Int J Biol Macromol 164:4218–4230. https://doi.org/10.1016/j.ijbiomac.2020.08.201

Jena G, Anandkumar B, Vanithakumari SC, George RP, Philip J, Amarendra G (2020) Graphene oxide-chitosan-silver composite coating on Cu-Ni alloy with enhanced anti-corrosive and antibacterial properties suitable for marine applications. Prog Org Coatings 139:105444. https://doi.org/10.1016/j.porgcoat.2019.105444

Karimi AR, Tarighatjoo M, Nikravesh G (2017) 1,3,5-Triazine-2,4,6-tribenzaldehyde derivative as a new crosslinking agent for synthesis of pH-thermo dual responsive chitosan hydrogels and their nanocomposites: Swelling properties and drug release behavior. Int J Biol Macromol 105:1088–1095. https://doi.org/10.1016/j.ijbiomac.2017.07.128

Latifi N, Asgari M, Vali H, Mongeau L (2018) A tissue-mimetic nano-fibrillar hybrid injectable hydrogel for potential soft tissue engineering applications. Sci Rep 8:1–18. https://doi.org/10.1038/s41598-017-18523-3

Leung HW (2001) Ecotoxicology of glutaraldehyde: Review of environmental fate and effects studies. Ecotoxicol Environ Saf 49:26–39. https://doi.org/10.1006/eesa.2000.2031

Lin S, Chen L, Huang L, Cao S, Luo X, Liu K (2015) Novel antimicrobial chitosan-cellulose composite films bioconjugated with silver nanoparticles. Ind Crops Prod 70:395–403. https://doi.org/10.1016/j.indcrop.2015.03.040

Liu T, Li Y, Du Q, Sun J, Jiao Y, Yang G, Wang Z, Xia Y, Zhang W, Wang K, Zhu H, Wu D (2012) Adsorption of methylene blue from aqueous solution by graphene. Colloids Surf B Biointerfaces 90:197–203. https://doi.org/10.1016/j.colsurfb.2011.10.019

Mittal G, Rhee KY, Park SJ, Hui D (2017) Generation of the pores on graphene surface and their reinforcement effects on the thermal and mechanical properties of chitosan-based composites. Compos Part B Eng 114:348–355. https://doi.org/10.1016/j.compositesb.2017.02.018

Mokhothu TH, John MJ (2015) Review on hygroscopic aging of cellulose fibres and their biocomposites. Carbohydr Polym 131:337–354. https://doi.org/10.1016/j.carbpol.2015.06.027

Muthuchamy M, Govindan R, Shine K, Thangasamy V, Alharbi NS, Thillaichidambaram M, Khaled JM, Wen JL, Alanzi KF (2020) Anti-biofilm investigation of graphene/chitosan nanocomposites against biofilm producing P. aeruginosa and K. pneumoniae. Carbohydr Polym. https://doi.org/10.1016/j.carbpol.2019.115646

Özer D, Dursun G, Özer A (2007) Methylene blue adsorption from aqueous solution by dehydrated peanut hull. J Hazard Mater 144:171–179. https://doi.org/10.1016/j.jhazmat.2006.09.092

Pinheiro HM, Touraud E, Thomas O (2004) Aromatic amines from azo dye reduction: status review with emphasis on direct UV spectrophotometric detection in textile industry wastewaters. Dye Pigment 61:121–139. https://doi.org/10.1016/j.dyepig.2003.10.009

Rasoulzadehzali M, Namazi H (2018) Facile preparation of antibacterial chitosan/graphene oxide-Ag bio-nanocomposite hydrogel beads for controlled release of doxorubicin. Int J Biol Macromol 116:54–63. https://doi.org/10.1016/j.ijbiomac.2018.04.140

Reghioua A, Barkat D, Jawad AH, Abdulhameed AS, Al-Kahtani AA, Al-Othman ZA (2021) Parametric optimization by Box-Behnken design for synthesis of magnetic chitosan-Benzil/ZnO/Fe3O4 nanocomposite and textile dye removal. J Environ Chem Eng. https://doi.org/10.1016/j.jece.2021.105166

Rodríguez-González C, Martínez-Hernández AL, Castanõ VM, Kharissova OV, Ruoff RS, Velasco-Santos C (2020) Polysaccharide nanocomposites reinforced with graphene oxide and keratin-grafted graphene oxide. Ind Eng Chem Res 51:3619–3629. https://doi.org/10.1021/ie200742x

Sharma A, Thakur M, Bhattacharya M, Mandal T, Goswami S (2019) Commercial application of cellulose nano-composites – A review. Biotechnol Rep 21:e00316. https://doi.org/10.1016/j.btre.2019.e00316

Siburian R, Sihotang H, Lumban Raja S, Supeno M, Simanjuntak C (2018) New route to synthesize of graphene nano sheets. Orient J Chem 34:182–187. https://doi.org/10.13005/ojc/340120

Stefanescu C, Daly WH, Negulescu II (2012) Biocomposite films prepared from ionic liquid solutions of chitosan and cellulose. Carbohydr Polym 87:435–443. https://doi.org/10.1016/j.carbpol.2011.08.003

Tang F, Yu H, Abdalkarim SYH, Sun J, Fan X, Li Y, Zhou Y, Tam KC (2020) Green acid-free hydrolysis of wasted pomelo peel to produce carboxylated cellulose nanofibers with super absorption/flocculation ability for environmental remediation materials. Chem Eng J 395:125070. https://doi.org/10.1016/j.cej.2020.125070

Toeri J, Osorio-Madrazo A, Laborie MP (2017) Preparation and chemical/microstructural characterization of azacrown ether-crosslinked chitosan films. Mater (basel). https://doi.org/10.3390/ma10040400

Tran CD, Mututuvari TM (2015) Cellulose, chitosan, and keratin composite materials. Controlled Drug Release. https://doi.org/10.1021/la5034367

Tran CD, Duri S, Delneri A, Franko M (2013) Chitosan-cellulose composite materials: preparation, characterization and application for removal of microcystin. J Hazard Mater 252–253:355–366. https://doi.org/10.1016/j.jhazmat.2013.02.046

Udoetok IA, Wilson LD, Headley JV (2016) Self-Assembled and Cross-Linked Animal and Plant-Based Polysaccharides: Chitosan-Cellulose Composites and Their Anion Uptake Properties. ACS Appl Mater Interfaces 8:33197–33209. https://doi.org/10.1021/acsami.6b11504

Valizadeh S, Naseri M, Babaei S, Hosseini SMH, Imani A (2019) Development of bioactive composite films from chitosan and carboxymethyl cellulose using glutaraldehyde, cinnamon essential oil and oleic acid. Int J Biol Macromol 134:604–612. https://doi.org/10.1016/j.ijbiomac.2019.05.071

Wang L, Zhang J, Wang A (2008) Removal of methylene blue from aqueous solution using chitosan-g-poly(acrylic acid)/montmorillonite superadsorbent nanocomposite. Colloids Surf A Physicochem Eng Asp 322:47–53. https://doi.org/10.1016/j.colsurfa.2008.02.019

Wang R, Shou D, Lv O, Kong Y, Deng L, Shen J (2017) pH-Controlled drug delivery with hybrid aerogel of chitosan, carboxymethyl cellulose and graphene oxide as the carrier. Int J Biol Macromol 103:248–253. https://doi.org/10.1016/j.ijbiomac.2017.05.064

Wu M, Chen W, Mao Q, Bai Y, Ma H (2019) Facile synthesis of chitosan/gelatin filled with graphene bead adsorbent for

orange II removal. Chem Eng Res Des 144:35–46. https://doi.org/10.1016/j.cherd.2019.01.027

Xu X, Yu J, Liu C, Yang G, Shi L, Zhuang X (2021) Xanthated chitosan/cellulose sponges for the efficient removal of anionic and cationic dyes. React Funct Polym 160:104840. https://doi.org/10.1016/j.reactfunctpolym.2021.104840

Yan L, Chen W (2011) Preparation of chitosan / graphene oxide composite film with enhanced mechanical strength in the wet state. Carbohydr Polym 83:653–658. https://doi.org/10.1016/j.carbpol.2010.08.038

Yang H, Sheikhi A, Van De Ven TGM (2016a) Reusable green aerogels from cross-linked hairy nanocrystalline cellulose and modified chitosan for dye removal. Langmuir 32:11771–11779. https://doi.org/10.1021/acs.langmuir.6b03084

Yang J, Duan J, Zhang L, Lindman B, Edlund H, Norgren M (2016b) Spherical nanocomposite particles prepared from mixed cellulose–chitosan solutions. Cellulose 23:3105–3115. https://doi.org/10.1007/s10570-016-1029-4

Yigit O, Dikici B, Senocak TC, Ozdemir N (2020) One-step synthesis of nano-hydroxyapatite/graphene nanosheet hybrid coatings on Ti6Al4V alloys by hydrothermal method and their in-vitro corrosion responses. Surf Coat Technol 394:125858. https://doi.org/10.1016/j.surfcoat.2020.125858

Zhang D, Wang L, Zeng H, Yan P, Nie J, Sharma VK, Wang C (2019) A three-dimensional macroporous network structured chitosan/cellulose biocomposite sponge for rapid and selective removal of mercury(II) ions from aqueous solution. Chem Eng J 363:192–202. https://doi.org/10.1016/j.cej.2019.01.127

Zhao L, Yang S, Yilihamu A, Ma Q, Shi M, Ouyang B, Zhang Q, Guan X, Yang ST (2019) Adsorptive decontamination of Cu2+-contaminated water and soil by carboxylated graphene oxide/chitosan/cellulose composite beads. Environ Res 179:108779. https://doi.org/10.1016/j.envres.2019.108779

Zhong Z, Qin J, Ma J (2015) Cellulose acetate/hydroxyapatite/chitosan coatings for improved corrosion resistance and bioactivity. Mater Sci Eng C 49:251–255. https://doi.org/10.1016/j.msec.2015.01.020